






Tunable photon-recoil forces and negative torque at flat-top beam edges

Received: 27 January 2025

Accepted: 16 September 2025

Published online: 22 October 2025

Fan Nan ^{1,2}✉, Xiao Li ^{3,4}, Siyuan Huang⁵, Shuailong Zhang ⁶, Jack Ng ⁴✉ & Yuebing Zheng ⁵✉

Tightly focused Gaussian beams are the cornerstone of traditional optical tweezers. Flat-top beams also enable consummate control of particles over a two-dimensional plane. The former depends on the intensity gradient, while the latter the phase gradient. Here we present a promising alternative for micro/nano-manipulation that complement the phase gradient force in a flat-top beam: utilizing the light-recoiling, particle can be reversibly manipulated or trapped, even along directions without phase or intensity gradients. Typically, these photon-recoil forces are dependent heavily on the details of the microscopic structures of matter, thus limiting both their tunability and reversibility. The photon-recoil-based manipulation technique (PMT) we develop utilizes polarization modulation to exert tunable and reversible lateral forces on simple nanospheres by shaping the imaginary Poynting momentum (IPM) in a flat-top beam. By harnessing recoil forces arising from IPM, our PMT creates edge-specific pathways, enabling tunable driving forces for nanoparticle transport and the formation of stable potential wells. Furthermore, PMT makes it possible to achieve negative optical torque on single nanowires, thereby overcoming previous limitations and opening different avenues in optical manipulation.

Optical manipulation techniques revolutionized our control over microscopic particles, enabling precise positioning and force actuation that catalyze advances in nanotechnology^{1–5}, materials science^{6–10}, and cellular biophysics^{11–14}. Optical tweezers rely primarily on intensity gradients to trap particles within a tightly focused optical field¹⁵. In sharp contrast, flat-top beams offer a solution for controlled manipulation of particles using phase-gradient forces. Previous techniques predominantly focus on light-matter interactions within the central region of the beam, where phase can be readily adjusted¹⁶. For example, the phase gradient of a flat-top beam has been effective in assembling and collectively manipulating multiple nanoparticles^{17,18}.

Specifically, these programmable gradients enable the optical transport of multiple plasmonic nanoparticles while simultaneously facilitating their electromagnetic interaction to form spinning optically bound dimers. Stable spinning dimers with controllable rotational and translational motion across a planar surface are also experimentally demonstrated¹⁸. More intriguingly, by tuning the global polarization, microstructures with asymmetric light-scattering properties can be rotated and transported via photon recoil, without the need for gradient forces^{19–22}. However, this dependence on recoil forces is heavily constrained by the specific structural design of the particles being manipulated, presenting a major limitation: the inability to produce

¹College of Physics & Optoelectronic Engineering, Institute of Nanophotonics, Jinan University, Guangzhou, China. ²Institute of Biological and Chemical Systems, Karlsruhe Institute of Technology, Eggenstein-Leopoldshafen, Germany. ³Department of Physics and Institute for Advanced Study, The Hong Kong University of Science and Technology, Hong Kong, China. ⁴Department of Physics, State Key Laboratory of Quantum Functional Materials, and Guangdong Basic Research Center of Excellence for Quantum Science, Southern University of Science and Technology, Shenzhen, Guangdong, China. ⁵Walker Department of Mechanical Engineering, Texas Materials Institute, and Materials Science and Engineering Program, The University of Texas at Austin, Austin, TX, USA. ⁶School of Integrated Circuits and Electronics, Beijing Institute of Technology, Beijing, China. ✉e-mail: fnan190730@gmail.com; wuzh3@sustech.edu.cn; zheng@austin.utexas.edu

position-dependent recoil forces with tunable magnitude and direction, which are crucial for creating stable trapping potentials akin to gradient forces. The potential of flat-top beams to generate tunable recoil forces that mimic the behavior of phase gradient^{17,18,23–26}, enhancing the precision and directionality of applied forces, even on unstructured particles, remains unexplored. Unlocking this capability is critical for advancing optical manipulation and developing different types of optical tweezers. In particular, it may open the door to the realization of practical negative optical force and torque^{5,21,27–38}—counterintuitive light-matter interactions that nonetheless comply with conservation laws and fundamental physical principles. Specifically, achieving these breakthroughs without the need for special materials and structures, or strict experimental conditions, while maintaining tunability and reconfigurability, represents a significant advance.

Here, we introduce a method to manage photon-recoil effects at the edges of a flat-top beam, unlocking possibilities for versatile nanomanipulation and complementing the phase-gradient forces in a flat-top beam. This method, referred to as the photon-recoil-based manipulation technique (PMT), circumvents the requirement for intensity or phase variations along the manipulation pathway by shaping the imaginary Poynting momentum (IPM) of the flat-top beam. As a result, it is applicable to normal nanoparticles without requiring specialized structural designs. PMT utilizes polarization modulation to generate lateral recoil forces that are both sign-reversible and magnitude-tunable. We demonstrate its ability to manipulate metallic nanospheres, enabling them to be transported, rotated, or stably

confined along the optical edges. Moreover, we demonstrated negative optical torques on single nanowires, a phenomenon that had been challenging to achieve in earlier studies. PMT represents a significant difference from traditional optical manipulation techniques, providing an adaptable and efficient platform for nanoparticle and nanowire manipulation. By enhancing the capabilities of flat-top beams, particularly by concentrating optical forces at their edges, PMT unlocks possibilities for applications demanding reconfigurable trapping, transport, and rotation.

Results and discussion

General concept and physics mechanism of the photon-recoil-based manipulation technique

Figure 1a shows a schematic illustrating the tunable and reversible transport of single nanoparticles along the edges of a flat-top beam, accomplished without the need for in-plane phase gradients and instead controlled solely by adjusting the polarization of light. We begin by demonstrating this concept with a linearly polarized beam. In this configuration, the polarization is globally modulated (e.g., using a waveplate), which enables precise control over the direction and magnitude of optical forces acting on a nanoparticle by simply tuning the polarization direction (Fig. 1b). These optical forces primarily act when the nanoparticle is positioned at the beam's edge, where intensity gradients exist. When the polarization aligns with the top and bottom optical edges (left panel of Fig. 1b), the force direction follows that of the intensity gradient, though the force magnitudes differ across adjacent sides. Interestingly, under diagonal polarization (the middle

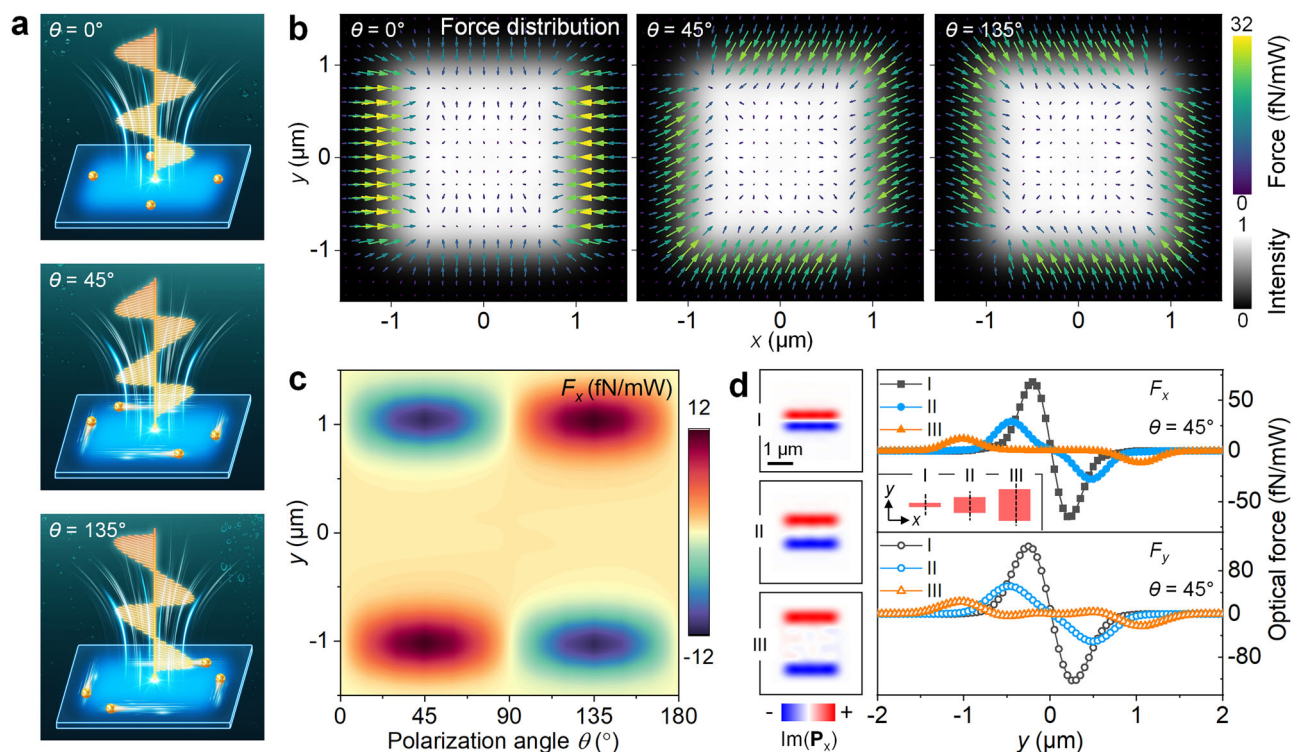


Fig. 1 | General concept and working principle of PMT. **a** Schematic of reversible transportation of single nanoparticles on the edges of a flat-top beam by solely tuning the linear polarization angle. **b** The intensity map of a flat-top beam at three representative polarization angles, where the calculated force applied on a single Au nanoparticle (300 nm in dia.) at various positions is overlaid on the map. When diagonal polarizations are used, a lateral force arises, oriented perpendicularly to the intensity gradients. The laser wavelength is 800 nm, and θ is defined as the angle between the polarization direction and the x-axis. **c** Calculated polarization angle-resolved lateral optical force (F_x) on an Au nanoparticle positioned at various y-coordinates, with the x-coordinate fixed at 0. **d** The evolution and origin of lateral

force. The inset illustrates three optical patterns of varying widths (I–III), showcasing the transition in the optical field's intensity profile from an elongated line to a two-dimensional planar configuration. This evolution corresponds to the separation of opposing imaginary Poynting vectors (left column) and the elimination of the intensity-gradient potential well along the y-axis. The imaginary Poynting momentum can induce a lateral recoil force via simple magnetoelectric interactions. Notably, the sign of the imaginary Poynting vectors is opposite to that of the recoil force, dictated by a prefactor determined by the polarizabilities of the particle.

and right panels of Fig. 1b), the optical forces gain an additional component perpendicular to the intensity gradient (i.e., the lateral optical force^{19–21,39–47}). To further check the induced lateral optical force (e.g., F_x), we calculate the polarization angle-resolved optical force on an Au nanoparticle positioned at various y -coordinates while holding its x -position fixed ($x = 0$, Fig. 1c). These results clearly show that this optical force reverses not only with changes in the polarization angle but also due to symmetry, such that the lateral force direction inverts on the opposite side.

To figure out the origin of these edge-specific and polarization-dependent forces, we consider the recoil force induced by the IPM of light^{40,42,48–51}. Recently, optical manipulation based on IPM unlocks possibilities beyond conventional optical tweezers (COT). In particular, the experimental demonstration of metallic microparticle rotation using high-order IPM marked a significant breakthrough⁵¹, catalyzing rapid advances in this emerging research direction. Under the dipole approximation, the optical force arising from the IPM can be expressed as⁵¹

$$\mathbf{F}_{\text{IPM}}^{(l)} = A_{l,1} \text{Im}(\mathbf{E}^* \times \mathbf{H}) = A_{l,1} \text{Im}(\mathbf{P}) \quad (1)$$

where $A_{l,1} = \frac{\mu k^4}{12\pi\epsilon c} \text{Im}(\gamma_{\text{elec}}^{(l)*} \gamma_{\text{mag}}^{(l)})$, with ϵ , μ , and c being the permittivity, permeability, and light speed in the background medium, respectively. We used

$$\begin{aligned} \gamma_{\text{elec}}^{(l)} &= \frac{4l(2l+1)!! \, i\pi\epsilon a_l}{l+1 \, k^{2l+1}}, \\ \gamma_{\text{mag}}^{(l)} &= \frac{4l(2l+1)!! \, i\pi b_l}{l+1 \, \mu k^{2l+1}}, \end{aligned} \quad (2)$$

to represent the electric and magnetic 2^l -polar polarizabilities, and they reduce to the electric and magnetic dipolar polarizabilities, respectively, as $l=1$. With the Mie coefficients⁵² a_l and b_l in Eq. (2), we have presented the force coefficient, $A_{l,1}$, as a function of the size of an Au particle in Fig. S1. At a diameter of 300 nm, the electric and magnetic dipole terms are dominant and determine the qualitative behavior of the IPM-induced force, thereby justifying our use of the dipole approximation. In this case, this negative coefficient ($A_{1,1}$), along with the IPM distribution predominantly localized at the beam edges (Fig. S2) and its polarization dependence (Fig. S3), offers a comprehensive explanation for the amplitude and direction of the forces depicted in Fig. 1b, c. For example, when the light polarization is aligned with the x -axis, the x -component of the IPM is concentrated at the left and right edges, with its direction opposing the intensity gradient (Fig. S2). In contrast, the y -component of the IPM is concentrated at the top and bottom edges, aligning with the intensity gradient. This explains the varying force magnitudes across adjacent edges, as shown in Fig. 1b (left column; also see Fig. S4). When the polarization is misaligned with the edges, such as under diagonal polarization, the x -component of the IPM shifts to the top and bottom edges (Fig. 1d), while the y -component shifts to the left and right edges, resulting in the emergence of lateral recoil forces (e.g., F_x along the x -axis).

For small particles, the lateral recoil force is typically weaker than the conventional radiation pressure. On the transverse plane, as the relative strength of different forces depends sensitively on the illumination and particle parameters, there are cases where the lateral force is dominating. In some configurations, the gradient force may be absent or negligible, such as in uniformly illuminated beams without spatial intensity variations. In such cases, recoil forces may play a more dominant role, as they do not rely on intensity gradients but rather on interference between induced electric and magnetic dipoles. For larger particles, the primary contribution of the optical force induced by the IPM may shift to the interference between higher-order multipoles^{5,51,53,54} (see Fig. S5 for the size-dependent lateral force). We also investigate the recoil force associated with different materials for

a single particle with a 300 nm diameter (Fig. S6). Our results show that the optical response depends strongly on the material and significantly influences the magnitude of the recoil force, thereby affecting the overall efficiency of the PMT.

Furthermore, Fig. 1d demonstrates that experimentally observing lateral forces in a tightly focused (one-dimensional) optical field is challenging, as the strong intensity gradient confinement prevents edge equilibrium—even though this is the simplest configuration we identified for generating an IPM-induced force. Transforming the flat-top line into a two-dimensional flat-top beam effectively eliminates this intensity-gradient potential well. For effective implementation of PMT, these optical edges are well separated to preserve the distinctness of the lateral force experienced by the nanoparticle (Fig. S7).

We also calculated the optical force acting on a single Au nanoparticle under circularly polarized illumination (Fig. S8), where spin-orbit interaction is expected to play a role. The force is primarily concentrated at the beam's edge, accompanied by a lateral component that is perpendicular to the intensity gradient. By examining both the real and imaginary parts of the Poynting vector, we propose that this lateral component arises from contributions of both.

Edge-specific recoil force and direct experimental evidence under linear polarization

PMT demonstrates remarkable adaptability, working not only for simple square designs but also for customized geometries (Fig. 2a). These designs underline the robustness of PMT against a variety of perturbations, including defects or voids within the optical pattern. Our investigation of controlled voids revealed that these low-intensity regions act as additional boundaries. Notably, lateral forces can also arise along these new edges, with their direction reversing as the particle moves between parallel edges within the optical pattern. Furthermore, introducing central defects (hollow structures) does not alter the force distribution along the outer edges, ensuring that edge-guided particles follow predictable trajectories despite perturbations in the trap's central region.

To experimentally show that Au nanoparticles can be guided along two parallel edges in opposite directions under diagonal polarization, we introduce phase gradients into the flat-top beam (Fig. 2b). As illustrated in Fig. 1d, increasing the pattern width effectively disrupts the intensity-gradient potential well. While this alteration allows the nanoparticle to experience a consistent lateral optical force, achieving a stable lateral force (F_x) remains challenging due to the lack of an equilibrium position along the y -axis. Parabolic phase gradients within the flat-top beam effectively address this issue. These phase gradients provide a stable restoring force that directs particles toward the top and bottom edges, re-establishing equilibrium y -positions at those edges (Fig. 2c, d). We also check the impact of the optical phase gradient on the lateral force, analyzing how phase variations influence the magnitude and direction of the forces exerted on the particles (Fig. S9).

Figure 2e presents the measured dark-field images of multiple Au nanoparticles driven by such a flat-top beam over time (also see Video S1). Initially, these nanoparticles are confined within a defocused Gaussian beam, where they self-assemble into an ordered array due to strong optical binding interactions⁵⁵. Upon switching the optical pattern to a flat-top beam with a parabolic phase profile, as shown in Fig. 2b, the ordered array disperses, and individual particles are transported toward the top edge of the beam along the y -axis. After reaching the edge, a unidirectional lateral force directs the particles along the x -axis, causing them to move steadily across the field. During this period, from $t = 0.11$ s to $t = 0.23$ s, the number of particles gradually decreases as they exit the optical region. Moreover, the phase gradient of the flat-top beam can be precisely tuned to regulate the separation of nanoparticles. Figure 2f illustrates the simulated trajectories of two Au nanoparticles within a phase-gradient flat-top beam,

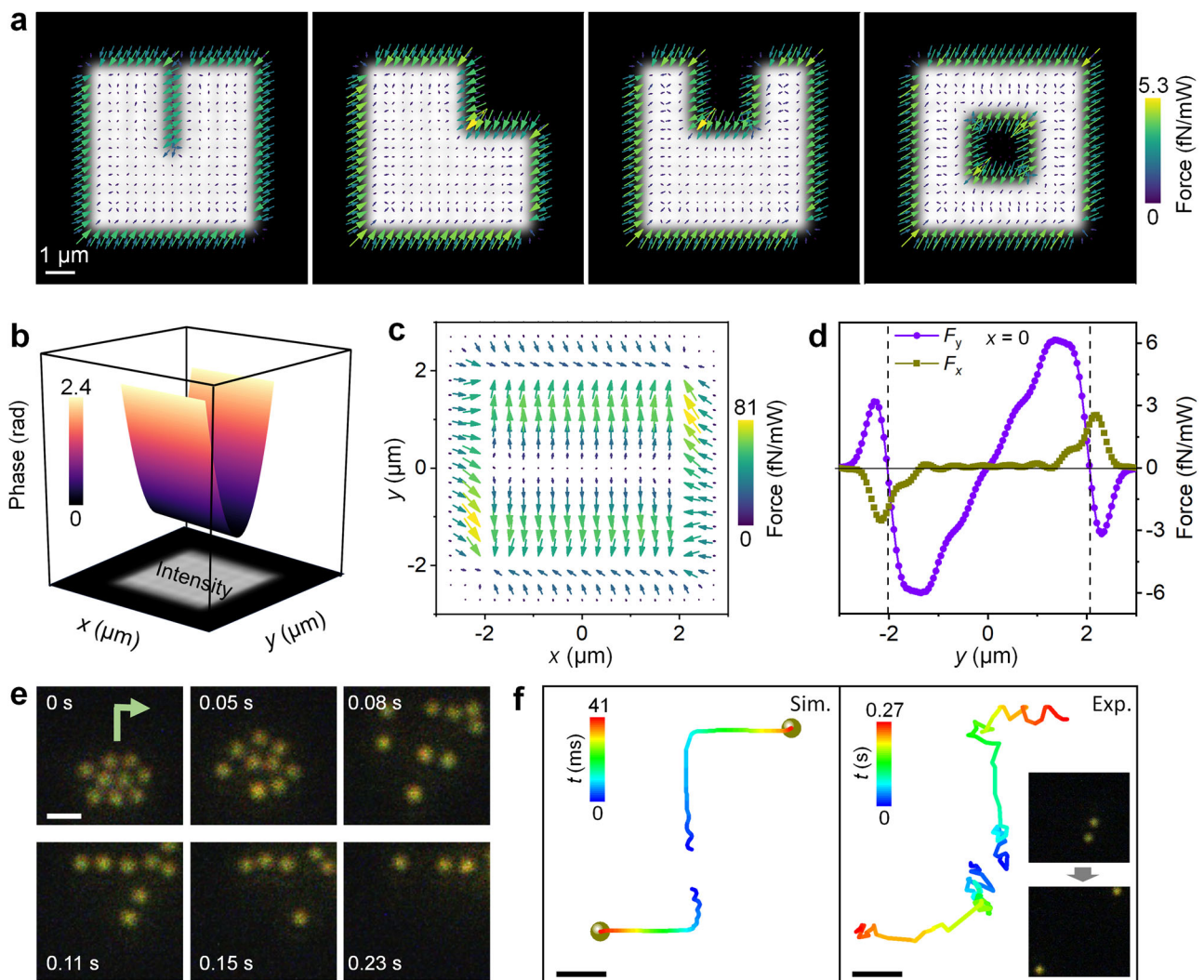


Fig. 2 | Edge-specific lateral force and direct experimental evidence. **a** The intensity map of a flat-top beam with various shapes, overlaid with the calculated forces acting on a single Au nanoparticle (300 nm in dia.) at different positions. The polarization angle is 45° . **b** Design of a flat-top beam with a parabolic phase profile. **c** The corresponding forces map of an Au nanoparticle. The polarization angle is -45° . **d** Equilibrium y -positions (indicated by dashed lines) are created at the top

and bottom edges of the optical field through the synergy of intensity and phase gradients, enabling lateral forces (F_x) to be detected by the particle. **e** Dark-field images of multiple nanoparticles driven by the phase gradient to experience lateral force on the edge. **f** Simulated and measured trajectories of two Au nanoparticles in a phase-gradient flat-top beam with a polarization angle of -45° . The scale bars are 1 μm .

showing a slight shift in their separation position toward the $-y$ direction. Experimental results, presented in the right panel of Fig. 2f (also see Video S2), confirm the simulation. By effectively combining lateral forces with phase-gradient forces, PMT facilitates controlled, bidirectional movement along parallel pathways.

Versatility of PMT in manipulating nanoparticle pathways and tuning trapping locations within a flat-top beam

A key feature of PMT is its capability to generate tunable trapping potentials at the edges of a flat-top beam. By incorporating polarization gradients⁵⁶, we reverse the recoil force along the optical edges, enabling precise trapping and guiding of nanoparticles. Figure 3a shows a flat-top beam with a polarization angle modulated along the x -axis, gradually shifting from -90° to 90° . To achieve this polarization variation while preserving a uniform intensity profile, two orthogonal polarization components are precisely designed with intensity modulations following cosine and sine functions along the x -axis, respectively (see Method section). The calculated distribution of $-\text{Im}(\mathbf{P})$ shown in Fig. 3b reveals that the lateral force along the top edge of the field reverses direction as expected, creating a potential well at the

center of the top edge (Fig. 3c, also see Fig. S10A for the creation of a potential well at the corner). At the same time, this polarization profile creates lateral recoil forces in the beam's central region, which also arises from IPM (Fig. 3b). These forces act similarly to the phase-gradient effect seen in Fig. 2b, guiding the particle to the edge (Fig. S11). Even in the absence of in-plane phase gradients, polarization modulation alone causes the nanoparticle to be repelled from the central region and eventually trapped at the top edge of the pattern (Fig. 3c; also see Video S3 for the experimental results). It should be noted that our PMT cannot fully replicate the functionalities of the powerful phase gradients within a flat-top beam^{17,18}. Nevertheless, PMT is believed to complement phase-gradient-based optical manipulation by introducing a fundamentally different strategy that enables tunable photon recoil via IPM shaping, offering another degree of control over optical forces and particle dynamics.

By simply switching the polarization states of the two orthogonal components, the polarization angle gradually shifts from -180° to 0° (Fig. 3d). This adjustment leads to the emergence of two potential wells positioned at opposite corners of the optical field (Fig. 3e, also see Fig. S10B for the creation of two potential wells at the same edge).

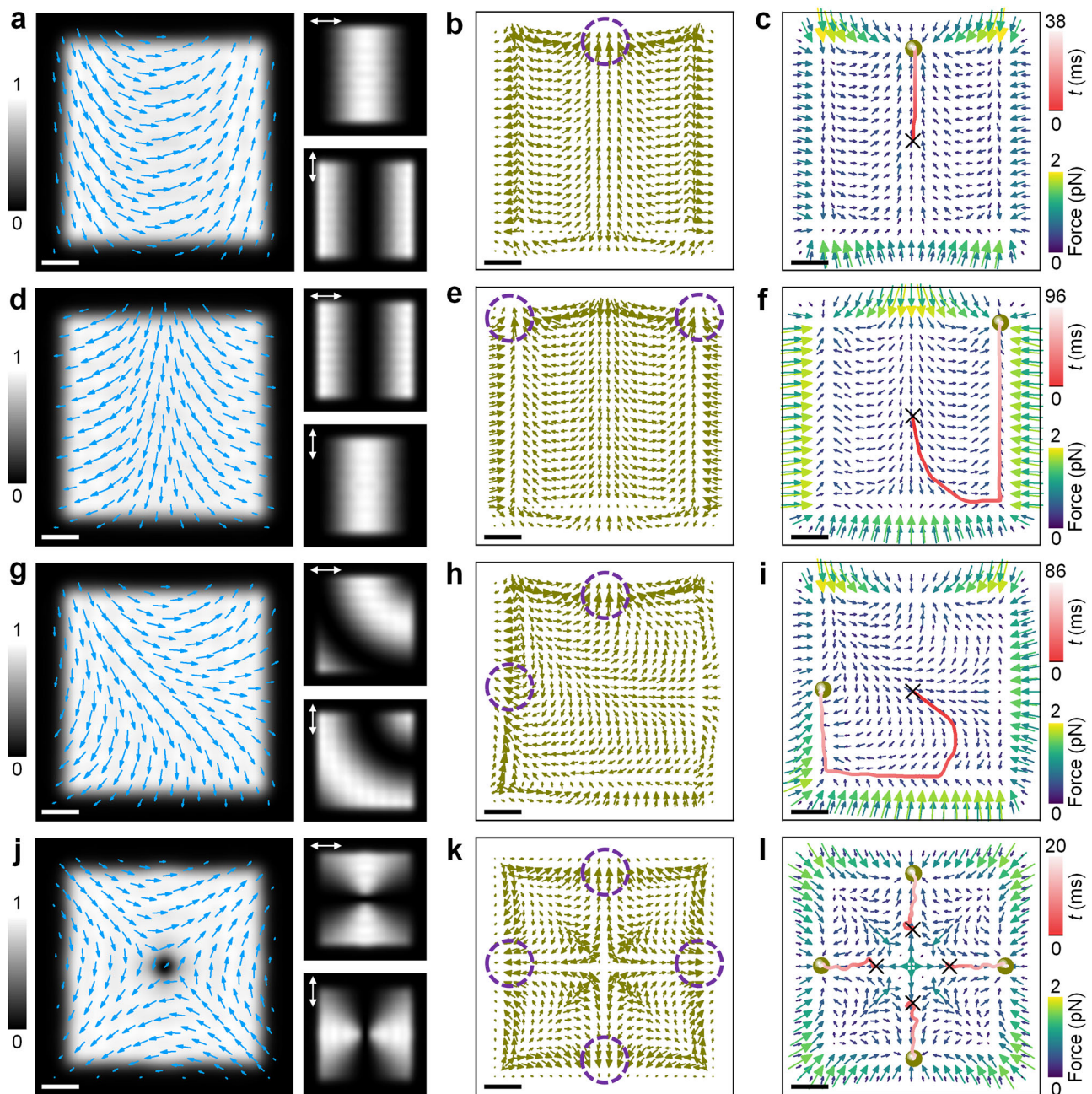


Fig. 3 | Tunable optical trapping of single nanoparticles. **a, d, g, j** Electric field vectors (blue arrows) of four flat-top beams, alongside the intensity profiles of their two orthogonal polarization components. **b, e, h, k** Calculated $-\text{Im}(\mathbf{P})$ corresponding to the beams in (**a, d, g, j**), respectively. **c, f, i, l** Calculated force maps for a single Au nanoparticle (300 nm diameter) and the corresponding trajectories of Au nanoparticles within the four distinct optical fields. The laser power is 400 mW.

a–c A single potential well forms at the top edge of the pattern. **d–f** Two potential wells are created at two corners of the pattern. **g–i** Two potential wells appear at adjacent edges of the pattern. **j–l** Four potential wells are generated, with a central void caused by polarization singularity. These stable trapping potential wells are marked by dashed circles. The scale bars are 1 μm .

The simulated trajectory of the same particle, initially positioned at the center of the beam, reveals a new path, showing how the particle is redirected toward one of the potential wells (Fig. 3f, also see Video S4 for the experimental results).

To demonstrate the versatility of PMT in manipulating nanoparticle pathways and tuning trapping locations and potentials, we design a flat-top beam with other polarization profiles. By introducing additional polarization modulation along the y-axis (Fig. 3g), a new potential well is created at the adjacent edge (Fig. 3h), with a wider profile compared to the potential well at the top edge (also see Fig. S12). The same nanoparticle transitions

from the beam center to the new potential well along a distinct pathway (Fig. 3i; also see Video S5 for the experimental results). Moreover, a specific polarization profile gives rise to a central void with reduced intensity, caused by a polarization singularity (Fig. 3j), along with the formation of four potential wells, one at each edge (Fig. 3k). The corresponding simulated trajectories show the simultaneous transport and trapping of four Au nanoparticles, each guided toward an edge of the optical pattern (Fig. 3l, also see Video S6). These results also show that the number of equilibrium trapping positions in a flat-top beam dictates its division into regions, with particles in each region drawn to their

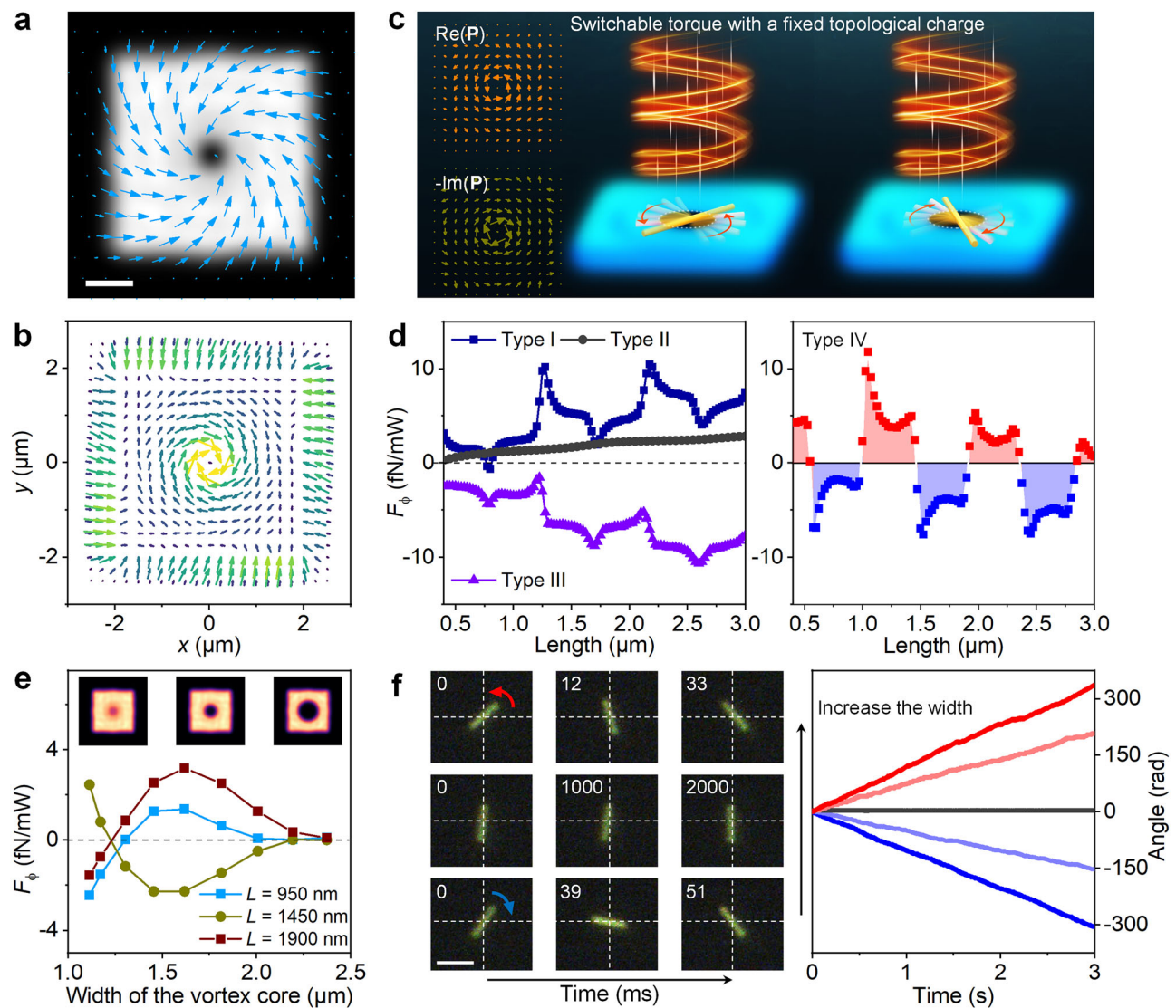


Fig. 4 | Negative optical torque in single Au nanowires. **a** Electric field vectors of another type of flat-top beam. This beam is generated by superimposing two flat-top beams: one with radial polarization and the other with azimuthal polarization. The central void results from the polarization singularity. **b** Calculated force map of a single Au nanoparticle (300 nm in dia.) corresponding to (a). **c** Schematic of reversible rotation of a single Au nanowire by introducing a competition between the azimuthal phase-gradient force and the recoil force induced by IPM. **d** Calculated optical-driven force (i.e., the azimuthal force) as a function of wire length under different types of optical patterns. The diameter of the nanowires is fixed at 100 nm. Types I and II represent two linearly polarized beams with azimuthal phase gradient (topological charge $l = -1$) whose polarization directions are along the x -axis and y -axis, respectively. Types III and IV represent two vector beams

(whose polarization vectors spiral around the singular point) without (topological charge $l = 0$) and with azimuthal phase gradients (topological charge $l = -1$), respectively. The orientation of the nanowire is along the x -axis. These optical fields have the same intensity profiles. **e** Calculated azimuthal force illustrates how modulation of the intensity profile, specifically the vortex core width, in the Type IV optical pattern enables bidirectional rotation of single nanowires. **f** Dark-field images and measured angular trajectories of a single Au nanowire in type IV optical patterns with different vortex core widths. Note that the driven force is defined as the net optical force exerted on one half of the nanowire, with the nanowire positioned at the center of the optical field. This force is evaluated along the direction perpendicular to the nanowire's long axis, that is, in the azimuthal direction relative to the beam center. The scale bars are 1 μm .

respective potential wells—enabling long-range manipulation beyond that of conventional intensity-gradient traps.

Furthermore, the spiral-like polarization profile (Fig. 4a) induces unidirectional forces along the edge. Compared to the outer edge, the central region exerts significantly stronger rotational forces in the opposite direction, as confirmed by the corresponding force map for a single Au nanoparticle (Fig. 4b). Additionally, the central void is tunable and can attain dimensions substantially larger than those resulting from polarization singularities (also see Fig. S13 and Video S7). These results motivate us to explore an advanced level of control facilitated by PMT, specifically the realization of negative optical force and torque. This mechanism relies on the creation of momentum flow along the field's edges via photon

recoil, which competes with the linear or angular momentum transfer induced by additional phase gradients.

We find that the force and torque exerted on a single Au nanosphere are position-dependent. In the central region of the optical field, the optical force is dominated by the phase-gradient force, whereas at the edges, it is governed by the recoil force (Fig. S14). Consequently, for larger particles, such as nanowires, which can simultaneously interact with both the edge and inner regions of the flat-top beam, negative torque may become achievable (Fig. 4c). We first check the azimuthal driven force as a function of the nanowire's rotation angle relative to the linear polarization direction, while holding the nanowire length constant in a flat-top beam with a topological charge of -1 . This allows us to investigate how angular

alignment affects the force exerted on the nanowire^{57,58}, specifically in the context of a beam configuration where orbital angular momentum is present. The force reaches its maximum when the orientation of the nanowire is aligned parallel to the polarization angle (Fig. S15A, C).

The demonstration of negative optical torque on a single nanowire via PMT

Figure 4d illustrates the calculated optical driving force acting on single Au nanowires of varying lengths. Types I and II represent two flat-top beams, each with a topological charge of -1 but differing in linear polarization orientations. In these calculations, the orientation of the nanowire is fixed, leading to two distinct cases that yield significantly different optical driving forces based on the nanowire's alignment with the polarization angle. When the nanowire is oriented perpendicular to the polarization angle (type II pattern), the force profile is smooth because only the transverse mode of the nanowire is excited. In contrast, when the nanowire is parallel to the polarization angle (type I pattern), the interaction of light with the Fabry–Pérot and Mie resonances gives rise to multipole modes, resulting in abrupt changes in the force profile due to these resonant interactions^{44,46}. Overall, the optical driving force is predominantly positive, as expected, with a few exceptions at specific nanowire lengths where resonance conditions lead to deviations. We then calculate the length-dependent driven force when changing the optical pattern to that shown in Fig. 4a (type III). Similar to previous observations, the abrupt changes in the force profile are attributed to the emergence of these multipole resonances. Notably, the sign of the forces is opposite to that observed in types I and II, as expected.

The type IV beam is generated by introducing an azimuthal phase gradient into the type III beam (also see Fig. S16 for a comparison of intensity profiles from type I to type IV). This configuration creates an interplay between the recoil forces at the boundary and the phase-gradient forces in the inner region, resulting in a competitive force environment that enables precise control over nanowire rotation. Results show that under the influence of a type IV optical pattern, multiple crossovers occur between positive and negative optical-driven forces as a function of the nanowire length (right panel of Fig. 4d). The angular dependence of the optically driven force applied on a single Au nanowire remains constant, enabling stable rotation of the nanowire (distinct from the behavior observed in type I or type II optical patterns, also see Fig. S15B, C).

More interestingly, we find that adjusting the void size of a type IV optical pattern, as shown in the insert of Fig. 4e (For simplicity, we set a dashed line to clearly define the width of the vortex core, also see Figs. S17 and S18), enables control over both the sign and magnitude of the optical torque: a previously unexplored paradigm in optical torque manipulation. Figure 4e presents the calculated azimuthal optical force as a function of the void size (i.e., the width of the vortex core). By increasing the core width, we can finely tune the balance between the positive azimuthal phase-gradient force and the negative recoil optical force, achieving a reversible optical-driven force. This dependency on the void size also interacts with the nanowire length. The experimental results, shown in Fig. 4f, illustrate the dark-field images and rotation angles of the same nanowire over time, demonstrating adjustable rotation speed and direction (Video S8). These observations align closely with our theoretical predictions, confirming the effectiveness of tuning the optical torque by modifying the void size (see method section).

We further explored the effect of higher topological charges (e.g., $l = -2$) on the optical torque experienced by nanowires of varying lengths and diameters (Fig. S19). Increasing the topological charge generally reduces the likelihood of achieving negative torque, due to the enhanced azimuthal phase gradient along the positive direction. However, negative torque was still observed for nanowires of a certain length and diameter.

We also investigate the tuning of the optical driving force on a single nanowire using radially symmetric phase gradients. By incorporating a radially symmetric phase gradient into a flat-top beam with spiral-shaped polarization distributions, we find that adjusting the sign of the phase gradient affects the optical driving forces exerted on nanowires of varying lengths (Fig. S20). When the sign of the phase gradient is positive, with the phase profile forming a paraboloid distribution where the central region has a lower phase than the outer areas, the optical pattern generates a significantly stronger optical driving force compared to a pattern without any in-plane phase gradient. Conversely, when the sign is negative, a reduction in the driving force is observed. This behavior is similar to the light-driven effects in self-assembled nanoparticle arrays observed in our previous work¹⁷.

Moreover, PMT could be applied to the collective manipulation of multiple nanoparticles, enabling the assembly and rotation of self-organized particle clusters. Traditionally, the optical rotation of such clusters requires circularly polarized light to induce spin-orbit coupling^{17,32,33,59,60}. However, PMT enables the optical rotation of assembled microstructures without relying on the spin or orbital angular momentum of light (Video S9), thereby allowing the generation of negative optical torque, similar to the case observed with nanowires. Considering only the central particles in the array experience recoil forces that contribute to negative rotation, strong inter-particle interactions are essential for transmitting this torque and driving the rotation of the entire self-assembled structure. However, our previous experiments¹⁷ showed that the optical binding strength was insufficient, and nanoparticles failed to self-assemble into stable optical matter within a flat-top beam carrying an azimuthal phase gradient, even at low topological charge (e.g., $l = -1$). We conducted theoretical calculations for optical matter arrays fixed on a substrate (so that the particles are considered stable there, irrespective of the optical force). It is then clear that it is feasible to realize negative optical torque in optical matter arrays (e.g., comprising 7 or 19 particles, also see Fig. S21).

In our current setup, PMT operates in a two-dimensional configuration, where the strong radiation pressure in the third direction is counterbalanced by electrostatic interactions between the particle and the substrate. To achieve three-dimensional manipulation, we propose incorporating a reflective surface to generate interference, thereby creating a stable equilibrium position along the z -axis (Fig. S22).

Last but not least, PMT and COT serve distinct purposes, each with unique advantages. PMT utilizes precise polarization control to generate edge-specific forces, enabling advanced functionalities such as bidirectional transportation and nanoparticle confinement at field boundaries. Unlike COT, PMT is less dependent on central beam quality. However, the implementation of PMT necessitates complex beam shaping techniques, high-precision optical alignment, and the use of advanced optical components, such as spatial light modulators (SLMs), which collectively increase the overall complexity and cost of the system. Moreover, conventional SLMs are typically limited to modulating beams with specific incident polarizations, further constraining the flexibility of the optical setup. Nevertheless, recent advances in optical metasurfaces present promising opportunities to simplify PMT systems^{61–63}. By designing metasurfaces capable of directly generating polarization-tunable flat-top beams, it may become possible to eliminate the need for SLMs altogether. Such metasurfaces can provide both polarization control and beam shaping within a compact, static optical element, significantly reducing alignment requirements and system complexity. This development has the potential to streamline the PMT setup, enhance robustness, and improve scalability, thereby increasing its applicability in practical scenarios such as integrated photonic systems and lab-on-chip platforms.

Compared with other emerging optical manipulation techniques that also use polarization, PMT offers a unique set of advantages.

Plasmonic tweezers⁶⁴, for example, use surface plasmon resonances to achieve strong field enhancement and sub-wavelength trapping near metallic nanostructures. While highly effective at the nanoscale, plasmonic tweezers are often limited by localized heating and typically require surface-bound configurations, restricting their applicability in dynamic, volumetric manipulation. Optoelectronic tweezers (OET), by contrast, utilize light-induced virtual electrodes to generate dielectrophoretic forces⁶⁵. Although OET is well-suited for parallel manipulation of microscale particles, it generally lacks the spatial precision and flexibility required for nanoscale applications. In this context, our PMT bridges the gap between high-precision optical trapping and reconfigurable manipulation, offering a versatile platform for dynamic control of micro- and nanoparticles, particularly in scenarios where spatially tailored force landscapes are essential.

In summary, the PMT we developed represents a previously unexplored paradigm for nanomanipulation at the edges of flat-top beams. It is a robust and versatile technique that enables polarization-modulated control of motion and precise particle positioning by leveraging a tunable photon-recoil effect, a capability that was previously difficult to achieve. Even with global polarization modulation, such as simple linear polarization at a 45-degree angle, PMT allows bidirectional transport of individual nanoparticles exclusively along the beam edges. Under specific polarization profiles, PMT enables the formation of multiple stable trapping positions with varying stiffnesses. Moreover, we demonstrate the potential of PMT for generating negative optical torque in nanowires, revealing its complex interaction in rotational dynamics with a nanowire of finite length. By adjusting the central void of the flat-top beam, PMT enables switchable optical torque, showcasing its capacity for precise, length-specific control of nanostructures in optomechanical systems. The versatility of PMT establishes it as a powerful and adaptable tool for a wide range of experimental applications, offering transformative opportunities for edge-focused optical manipulation.

Methods

Calculating the optical force and particle trajectories. Numerical simulations were performed using Lumerical FDTD Solutions. To simulate the designed beam at the focal plane of an objective lens, we first calculate the intensity and phase profile of the optical field at the back aperture of the lens^{17,18,66}. The electric field components, E_x and E_y , were obtained and imported into the simulation environment via the “Import Source” function. As the fields propagate along the z -axis, the designed optical field is reconstructed at a focal plane located $2.16\ \mu\text{m}$ from the import source plane (Fig. S23). The source size was set to $10\ \mu\text{m}$, yielding a numerical aperture (NA) of ~ 1.2 , calibrated to align with experimental parameters. By combining two orthogonal components of a flat-top beam with well-defined intensity and phase profiles, we can generate a flat-top beam with customizable polarization and phase, enabling tailored manipulation. Nanoparticles and nanowires were positioned in the x - y plane at fixed z -coordinates ($2.16\ \mu\text{m}$) and immersed in water. Optical forces on each particle were calculated using the Maxwell stress tensor method. To explore the dynamic behavior of the nanoparticles within the tailored optical field, we employed a coupled FDTD-Langevin dynamics approach. In this method, after calculating the optical forces acting on each nanoparticle, the nanoparticle velocities are determined and used to update their positions according to the 2D Langevin equations⁶⁷. This iterative simulation loop predicts the trajectories of nanoparticles over time, with optical forces recorded at each step for detailed analysis.

Analytical derivations of the IPM forces near the edge centers of a flat-top beam. In constructing the flat-top beam with specific linear polarization distributions, as depicted in Fig. 3a, d, g, j, the polarization near the edge centers of the flat-top beam is predominantly either x -polarized or y -polarized. Consequently, the electric fields can be

approximately expressed as

$$\mathbf{E} = \hat{\mathbf{e}}E(\mathbf{r}) \quad (3)$$

with $\hat{\mathbf{e}}$ denoting the approximately uniform polarization direction and $E(\mathbf{r})$ being the amplitude distribution of the electric field near the edge centers of a flat-top beam. Accordingly, the magnetic field has the form of

$$\mathbf{H} = \frac{-i}{k\mu_0} \nabla \times \mathbf{E} = \frac{-i}{k\mu_0} \nabla \times (\hat{\mathbf{e}}E(\mathbf{r})) = \frac{-i}{k\mu_0} \nabla E(\mathbf{r}) \times \hat{\mathbf{e}} \quad (4)$$

And the IPM force can be expressed as

$$\begin{aligned} \mathbf{F}_{\text{IPM}} &= C \text{Im}(\mathbf{E}^* \times \mathbf{H}) \\ &= C \text{Im} \left(\left[\hat{\mathbf{e}}E^*(\mathbf{r}) \right] \times \left[\frac{-i}{k\mu_0} \nabla E(\mathbf{r}) \times \hat{\mathbf{e}} \right] \right) \\ &= C \text{Im} \left(\frac{-i}{k\mu_0} E^*(\mathbf{r}) [\nabla E(\mathbf{r}) - \hat{\mathbf{e}}\hat{\mathbf{e}} \cdot \nabla E(\mathbf{r})] \right) \end{aligned} \quad (5)$$

Near the edges of the flat-top beam, the gradient term $\nabla E(\mathbf{r})$ has no component along the tangential direction of the edges. Therefore, $\nabla E(\mathbf{r})$ can be expressed as $\hat{\mathbf{v}}\partial_v E(\mathbf{r})$, where $\hat{\mathbf{v}}$ represents the unit vector normal to the edge. And Eq. (5) will have the form of

$$\mathbf{F}_{\text{IPM}} = C(\hat{\mathbf{v}} - \hat{\mathbf{e}}\hat{\mathbf{e}} \cdot \hat{\mathbf{v}}) \text{Im} \left(\frac{-i}{k\mu_0} E^*(\mathbf{r}) \partial_v E(\mathbf{r}) \right) \quad (6)$$

If only the tangential ($\hat{\mathbf{t}}$) IPM force is of interest, then we have

$$\begin{aligned} \hat{\mathbf{t}} \cdot \mathbf{F}_{\text{IPM}} &= C \hat{\mathbf{t}} \cdot (\hat{\mathbf{v}} - \hat{\mathbf{e}}\hat{\mathbf{e}} \cdot \hat{\mathbf{v}}) \text{Im} \left(\frac{-i}{k\mu_0} E^*(\mathbf{r}) \partial_v E(\mathbf{r}) \right) \\ &= -C \hat{\mathbf{t}} \cdot \hat{\mathbf{e}}\hat{\mathbf{e}} \cdot \hat{\mathbf{v}} \text{Re}(E^*(\mathbf{r}) \partial_v E(\mathbf{r})) \\ &= -C \hat{\mathbf{t}} \cdot \hat{\mathbf{e}}\hat{\mathbf{e}} \cdot \hat{\mathbf{v}} \frac{1}{k\mu_0 c n_b \epsilon_0} \partial_v I \\ &= -C \hat{\mathbf{t}} \cdot \hat{\mathbf{e}}\hat{\mathbf{e}} \cdot \hat{\mathbf{v}} \frac{c}{k n_b} \partial_v I \end{aligned} \quad (7)$$

where $I = \frac{cn_b\epsilon_0}{2} |E(\mathbf{r})|^2$ denotes the light intensity and n_b is the refractive index of the background medium. According to Eq. (7), the tangential IPM force arises only when the linear polarization direction ($\hat{\mathbf{e}}$) near the edges is neither aligned with nor perpendicular to the tangential direction ($\hat{\mathbf{t}}$). Furthermore, an intensity gradient ($\partial_v I$) must exist in the direction perpendicular to the tangential direction ($\hat{\mathbf{t}}$) for the IPM force to manifest. We also clarify that the lateral recoil force observed in our study is not attributed to a spin-curl mechanism^{68–71} (see Figs. S24–S26).

Instrumentation and materials. Our holographic optical tweezers system is built around a continuous-wave laser (Spectra-Physics 3900S, operated at 800 nm), two liquid-crystal-on-silicon spatial light modulators (LCOS-SLM, Hamamatsu X15213-02), and a custom-built microscope equipped with a super-apochromatic objective lens (Olympus UPLSAPO60XW, NA 1.2) (also see Figs. S27 and S28). A high-numerical-aperture dark-field condenser (Nikon MBL12000) was used for illumination, enabling visualization of the nanoparticles. The motions of the particles are captured using a CMOS camera (Point Grey Grasshopper3). Half-wave plates are used to adjust the global polarization state of the beam. To achieve localized polarization (i.e., vector beams) with a uniform intensity profile, we design two orthogonal polarization components with specific intensity modulations along the x -axis and y -axis, respectively. Each component's intensity modulation follows a distinct function, allowing precise control over the polarization distribution across the beam profile while maintaining consistent overall intensity (Figs. S28B and S29). A beam profiler is used to characterize the intensity profiles of the pattern. The sample

cell consists of two coverslips (purchased from Thorlabs), separated by a 100 μm spacer, creating a sealed chamber to contain the colloidal solution. Colloidal solutions of Au nanoparticles (300 nm in dia.) were purchased from Sigma-Aldrich, while Au nanowires (100 \pm 10 nm in diameter and 1 \pm 0.1 μm in length) were purchased from Nanopartz. Both were diluted with deionized water to achieve the desired concentration. Within the liquid sample cell, nanoparticles and nanowires are confined close to the substrate. This z-axis equilibrium is achieved by balancing the optical radiation pressure of the laser with electrostatic repulsion between the particle and the glass coverslip surface.

Data availability

Source data are provided with this paper. All other relevant data supporting the findings of this study are available from the corresponding author on request.

References

- Grier, D. G. A revolution in optical manipulation. *Nature* **424**, 810–816 (2003).
- Maragò, O. M., Jones, P. H., Gucciarini, P. G., Volpe, G. & Ferrari, A. C. Optical trapping and manipulation of nanostructures. *Nat. Nanotechnol.* **8**, 807–819 (2013).
- Vijayan, J. et al. Scalable all-optical cold damping of levitated nanoparticles. *Nat. Nanotechnol.* **18**, 49–54 (2023).
- Berthelot, J. et al. Three-dimensional manipulation with scanning near-field optical nanotweezers. *Nat. Nanotechnol.* **9**, 295–299 (2014).
- Chen, J., Ng, J., Lin, Z. & Chan, C. T. Optical pulling force. *Nat. Photonics* **5**, 531–534 (2011).
- Lin, L. et al. Opto-thermoelectric nanotweezers. *Nat. Photonics* **12**, 195–201 (2018).
- Shi, Y. et al. Chirality-assisted lateral momentum transfer for bidirectional enantioselective separation. *Light Sci. Appl.* **9**, 62 (2020).
- Chen, Z., Li, J. & Zheng, Y. Heat-mediated optical manipulation. *Chem. Rev.* **122**, 3122–3179 (2022).
- Gould, O. E. C. et al. Manipulation and deposition of complex, functional block copolymer nanostructures using optical tweezers. *ACS Nano* **13**, 3858–3866 (2019).
- Melzer, J. E. & McLeod, E. Assembly of multicomponent structures from hundreds of micron-scale building blocks using optical tweezers. *Microsyst. Nanoeng.* **7**, 45 (2021).
- Bustamante, C. J., Chemla, Y. R., Liu, S. & Wang, M. D. Optical tweezers in single-molecule biophysics. *Nat. Rev. Methods Prim.* **1**, 25 (2021).
- Li, X. et al. Optical tweeze-sectioning microscopy for 3D imaging and manipulation of suspended cells. *Sci. Adv.* **11**, ead3900 (2025).
- Heller, I., Hoekstra, T. P., King, G. A., Peterman, E. J. G. & Wuite, G. J. L. Optical tweezers analysis of DNA–protein complexes. *Chem. Rev.* **114**, 3087–3119 (2014).
- Mittasch, M. et al. Non-invasive perturbations of intracellular flow reveal physical principles of cell organization. *Nat. Cell Biol.* **20**, 344–351 (2018).
- Ashkin, A., Dziedzic, J. M., Bjorkholm, J. E. & Chu, S. Observation of a single-beam gradient force optical trap for dielectric particles. *Opt. Lett.* **11**, 288–290 (1986).
- Gao, D. et al. Optical manipulation from the microscale to the nanoscale: fundamentals, advances and prospects. *Light Sci. Appl.* **6**, e17039 (2017).
- Nan, F., Li, X., Zhang, S., Ng, J. & Yan, Z. Creating stable trapping force and switchable optical torque with tunable phase of light. *Sci. Adv.* **8**, eadd6664 (2022).
- Rodrigo, J. A., Franco, E. & Martínez-Matos, Ó. Surface laser traps with conformable phase-gradient optical force field enable multifunctional manipulation of particles. *Photonics Res.* **12**, 2088–2103 (2024).
- Tanaka, Y. Y. et al. Plasmonic linear nanomotor using lateral optical forces. *Sci. Adv.* **6**, eabc3726 (2020).
- Andrén, D. et al. Microscopic metavehicles powered and steered by embedded optical metasurfaces. *Nat. Nanotechnol.* **16**, 970–974 (2021).
- Wu, X. et al. Light-driven microdrones. *Nat. Nanotechnol.* **17**, 477–484 (2022).
- Engay, E. et al. Transverse optical gradient force in untethered rotating metaspinner. *Light Sci. Appl.* **14**, 38 (2025).
- Roichman, Y., Sun, B., Roichman, Y., Amato-Grill, J. & Grier, D. G. Optical forces arising from phase gradients. *Phys. Rev. Lett.* **100**, 013602 (2008).
- Yan, Z., Sajjan, M. & Scherer, N. F. Fabrication of a material assembly of silver nanoparticles using the phase gradients of optical tweezers. *Phys. Rev. Lett.* **114**, 143901 (2015).
- Nan, F. & Yan, Z. Sorting metal nanoparticles with dynamic and tunable optical driven forces. *Nano Lett.* **18**, 4500–4505 (2018).
- Rodrigo, J. A., Alieva, T., Manzaneda-González, V. & Guerrero-Martínez, A. All-optical trapping and programmable transport of gold nanorods with simultaneous orientation and spinning control. *ACS Nano* **18**, 27738–27751 (2024).
- Sukhov, S. & Dogariu, A. Negative nonconservative forces: optical “tractor beams” for arbitrary objects. *Phys. Rev. Lett.* **107**, 203602 (2011).
- Kajorndejnkul, V., Ding, W., Sukhov, S., Qiu, C.-W. & Dogariu, A. Linear momentum increase and negative optical forces at dielectric interface. *Nat. Photonics* **7**, 787–790 (2013).
- Sukhov, S. & Dogariu, A. On the concept of “tractor beams”. *Opt. Lett.* **35**, 3847–3849 (2010).
- Chen, J. et al. Negative optical torque. *Sci. Rep.* **4**, 6386 (2014).
- Hakobyan, D. & Brasselet, E. Left-handed optical radiation torque. *Nat. Photonics* **8**, 610–614 (2014).
- Sule, N., Yifat, Y., Gray, S. K. & Scherer, N. F. Rotation and negative torque in electrostatically bound nanoparticle dimers. *Nano Lett.* **17**, 6548–6556 (2017).
- Han, F. et al. Crossover from positive to negative optical torque in mesoscale optical matter. *Nat. Commun.* **9**, 4897 (2018).
- Li, X., Chen, J., Lin, Z. & Ng, J. Optical pulling at macroscopic distances. *Sci. Adv.* **5**, eaau7814 (2019).
- Shi, Y. et al. Inverse optical torques on dielectric nanoparticles in elliptically polarized light waves. *Phys. Rev. Lett.* **129**, 053902 (2022).
- Toftul, I. et al. Nonlinearity-induced optical torque. *Phys. Rev. Lett.* **130**, 243802 (2023).
- Xu, X. et al. Gradient and curl optical torques. *Nat. Commun.* **15**, 6230 (2024).
- Wang, N., Ng, J. & Wang, G. P. Morphology-independent general-purpose optical surface tractor beam. *Nat. Commun.* **15**, 6836 (2024).
- Wang, S. B. & Chan, C. T. Lateral optical force on chiral particles near a surface. *Nat. Commun.* **5**, 3307 (2014).
- Bliokh, K. Y., Bekshaev, A. Y. & Nori, F. Extraordinary momentum and spin in evanescent waves. *Nat. Commun.* **5**, 3300 (2014).
- Rodríguez-Fortuño, F. J., Engheta, N., Martínez, A. & Zayats, A. V. Lateral forces on circularly polarizable particles near a surface. *Nat. Commun.* **6**, 8799 (2015).
- Chen, H. et al. Lateral optical force due to the breaking of electromagnetic symmetry. *Phys. Rev. Lett.* **125**, 073901 (2020).
- Shi, Y. et al. Stable optical lateral forces from inhomogeneities of the spin angular momentum. *Sci. Adv.* **8**, eabn2291 (2022).
- Zhu, T. et al. Extraordinary multipole modes and ultra-enhanced optical lateral force by chirality. *Phys. Rev. Lett.* **125**, 043901 (2020).

45. Li, T. et al. Reversible lateral optical force on phase-gradient metasurfaces for full control of metavehicles. *Opt. Lett.* **48**, 255–258 (2023).
46. Nan, F. et al. Creating tunable lateral optical forces through multi-polar interplay in single nanowires. *Nat. Commun.* **14**, 6361 (2023).
47. Hayat, A., Mueller, J. P. B. & Capasso, F. Lateral chirality-sorting optical forces. *Proc. Natl. Acad. Sci. USA* **112**, 13190–13194 (2015).
48. Nieto-Vesperinas, M., Sáenz, J. J., Gómez-Medina, R. & Chantada, L. Optical forces on small magnetodielectric particles. *Opt. Express* **18**, 11428–11443 (2010).
49. Antognozzi, M. et al. Direct measurements of the extraordinary optical momentum and transverse spin-dependent force using a nano-cantilever. *Nat. Phys.* **12**, 731–735 (2016).
50. Xu, X. & Nieto-Vesperinas, M. Azimuthal imaginary Poynting momentum density. *Phys. Rev. Lett.* **123**, 233902 (2019).
51. Zhou, Y. et al. Observation of high-order imaginary Poynting momentum optomechanics in structured light. *Proc. Natl. Acad. Sci. USA* **119**, e2209721119 (2022).
52. Xu, Y. -I Electromagnetic scattering by an aggregate of spheres. *Appl. Opt.* **34**, 4573–4588 (1995).
53. Vercruysse, D. et al. Directional fluorescence emission by individual V-antennas explained by mode expansion. *ACS Nano* **8**, 8232–8241 (2014).
54. Vercruysse, D. et al. Unidirectional side scattering of light by a single-element nanoantenna. *Nano Lett.* **13**, 3843–3849 (2013).
55. Dholakia, K. & Zemánek, P. Colloquium: Grippled by light: optical binding. *Rev. Mod. Phys.* **82**, 1767–1791 (2010).
56. Lu, J., Ginis, V., Lim, S. W. D. & Capasso, F. Helicity and polarization gradient optical trapping in evanescent fields. *Phys. Rev. Lett.* **131**, 143803 (2023).
57. Shao, L. & Käll, M. Light-driven rotation of plasmonic nanomotors. *Adv. Funct. Mater.* **28**, 1706272 (2018).
58. Yan, Z. & Scherer, N. F. Optical vortex induced rotation of silver nanowires. *J. Phys. Chem. Lett.* **4**, 2937–2942 (2013).
59. Kudo, T., Yang, S.-J. & Masuhara, H. A single large assembly with dynamically fluctuating swarms of gold nanoparticles formed by trapping laser. *Nano Lett.* **18**, 5846–5853 (2018).
60. Cui, X., Mylnikov, V., Johansson, P. & Käll, M. Synchronization of optically self-assembled nanorotors. *Sci. Adv.* **10**, eadn3485 (2024).
61. Shen, K. et al. On-chip optical levitation with a metalens in vacuum. *Optica* **8**, 1359–1362 (2021).
62. Li, T. et al. Generation and conversion dynamics of dual Bessel beams with a photonic spin-dependent dielectric metasurface. *Phys. Rev. Appl.* **15**, 014059 (2021).
63. Song, Q., Liu, X., Qiu, C.-W. & Genevet, P. Vectorial metasurface holography. *Appl. Phys. Rev.* **9**, 011311 (2022).
64. Zhang, Y. et al. Plasmonic tweezers: for nanoscale optical trapping and beyond. *Light Sci. Appl.* **10**, 59 (2021).
65. Zhang, S. et al. Optoelectronic tweezers: a versatile toolbox for nano-/micro-manipulation. *Chem. Soc. Rev.* **51**, 9203–9242 (2022).
66. Rodrigo, J. A., Alieva, T., Abramochkin, E. & Castro, I. Shaping of light beams along curves in three dimensions. *Opt. Express* **21**, 20544–20555 (2013).
67. Nan, F., Han, F., Scherer, N. F. & Yan, Z. Dissipative self-assembly of anisotropic nanoparticle chains with combined electrodynamic and electrostatic interactions. *Adv. Mater.* **30**, 1803238 (2018).
68. Zhu, Y. et al. Mapping optical lateral forces on the Poincaré sphere. *ACS Photonics* **11**, 3267–3275 (2024).
69. Albaladejo, S., Marqués, M. I., Laroche, M. & Sáenz, J. J. Scattering forces from the curl of the spin angular momentum of a light field. *Phys. Rev. Lett.* **102**, 113602 (2009).
70. Ruffner, D. B. & Grier, D. G. Optical forces and torques in nonuniform beams of light. *Phys. Rev. Lett.* **108**, 173602 (2012).
71. Aloufi, K., Lembessis, V. E. & Aldossary, O. M. Revision of the forces exerted in the Rayleigh regime by a tightly focused optical vortex tweezer. *Phys. Rev. A* **109**, 023530 (2024).

Acknowledgements

The authors acknowledge the support from National Science Foundation of China (Nos. 12404361, 12074169), National Key Research and Development Program of China (2023YFE0112400), Guangdong Province Talent Recruitment Program (2021QN02C103), Research Grants Council of Hong Kong (AoE/P-502/20), Natural Science Foundation of Chongqing Municipality (2024NSCQ-JQX0192), Cullen Trust for Higher Education Endowed Professorship in Engineering #4.

Author contributions

F.N. conceived the idea, performed all the numerical simulations and optical experiments. J.N. and X.L. developed the analytical model to interpret the physics. S.H. and S.Z. assisted the experimental data analysis. F.N., J.N., and Y.Z. oversaw and directed the whole project. All authors discussed the results and contributed to the preparation of the manuscript.

Competing interests

The authors declare no competing interests.

Additional information

Supplementary information The online version contains supplementary material available at <https://doi.org/10.1038/s41467-025-64423-w>.

Correspondence and requests for materials should be addressed to Fan Nan, Jack Ng or Yuebing Zheng.

Peer review information *Nature Communications* thanks Baoli Yao and the other anonymous reviewer(s) for their contribution to the peer review of this work. [A peer review file is available].

Reprints and permissions information is available at <http://www.nature.com/reprints>

Publisher's note Springer Nature remains neutral with regard to jurisdictional claims in published maps and institutional affiliations.

Open Access This article is licensed under a Creative Commons Attribution-NonCommercial-NoDerivatives 4.0 International License, which permits any non-commercial use, sharing, distribution and reproduction in any medium or format, as long as you give appropriate credit to the original author(s) and the source, provide a link to the Creative Commons licence, and indicate if you modified the licensed material. You do not have permission under this licence to share adapted material derived from this article or parts of it. The images or other third party material in this article are included in the article's Creative Commons licence, unless indicated otherwise in a credit line to the material. If material is not included in the article's Creative Commons licence and your intended use is not permitted by statutory regulation or exceeds the permitted use, you will need to obtain permission directly from the copyright holder. To view a copy of this licence, visit <http://creativecommons.org/licenses/by-nc-nd/4.0/>.

© The Author(s) 2025